PAPER • OPEN ACCESS

Field validation of an actuated convergent-beam acoustic Doppler profiler for high resolution flow mapping

To cite this article: Samuel Harding *et al* 2021 *Meas. Sci. Technol.* **32** 045904

View the article online for updates and enhancements.

Field validation of an actuated convergent-beam acoustic Doppler profiler for high resolution flow mapping

Samuel Harding[1], **Mairi Dorward**[2] ⓘ, **Brian Sellar**[2] ⓘ and **Marshall Richmond**[1]

[1] Energy and Environment Directorate, Pacific Northwest National Laboratory, Richland, WA, United States of America

[2] Institute for Energy Systems, School of Engineering, The University of Edinburgh, Edinburgh, United Kingdom

E-mail: m.dorward@ed.ac.uk and brian.sellar@ed.ac.uk

CrossMark

Abstract

Energetic river and tidal flow environments feature complex hydrodynamic conditions. Conventional acoustic Doppler profiling instrumentation typically requires assumptions of flow homogeneity over the spatial scales of the divergent beam separation. This removes the ability to measure spatio-temporal variability within the flow. However, velocity variability within these spatial scales is often important in the design of structures and devices exposed to such flow, informing dynamic and peak hydrodynamic load predictions. The research presented outlines the development and testing of a flow measurement instrument consisting of multiple spatially-separated single beam acoustic Doppler profilers converging on a remote focal point, the location of which can be programmatically adjusted through actuation. This increases the spatial resolution at which remote field measurements can be made in energetic flow environments. Field testing of the instrument was conducted in a tidal channel at Sequim Bay Inlet, WA, USA. Results are compared with independent reference measurements made by a co-located, motion-corrected acoustic Doppler velocimeter. This comparison, across tidal velocities of 0.4–0.7 m s^{-1}, showed a mean velocity error of 0.5%–13.2% across nine sample locations within a 3.00 m × 2.25 m plane. To the authors' knowledge, this is the first publication of flow velocity results from non-intrusive acoustic measurements at an off-axis, focal point location that features 3D positional control.

Keywords: flow measurement, velocimetry, convergent acoustic Doppler profiler, renewable energy, tidal energy, marine hydro-kinetic energy

(Some figures may appear in colour only in the online journal)

1. Introduction

1.1. Background

Acoustic Doppler current profilers (ADCPs) measure flow velocities using the Doppler shift of backscattered acoustic signals from suspended particulate material in the water column. The motion of these particles approximates the velocity of the water particles and is therefore used as a proxy for the velocity of the local fluid flow. The transformation of velocity components from the beam direction of a diverging-beam ADCP to a 3D velocity vector in Cartesian coordinates depends on the assumption of flow homogeneity between multiple divergent beams at a given distance from the instrument. This is typically a valid assumption where mean flow velocity measurements are required for ocean current and open channel

flows. As such, ADCPs are often selected for remote velocity measurements given their ease of configuration, deployment and calibration. ADCPs have been deployed in rivers using both fixed and moving ADCPs to measure flow velocity (e.g. [1, 2]). The sensors are also utilised in tidal channel applications to measure mean flow [3, 4] and turbulence [5, 6] and investigate turbulence predictions from hydrodynamic models [7]. ADCPs are used in tidal energy applications to inform resource assessment [8], evaluate the performance of tidal turbines in the field [9, 10] and investigate turbine blade loading [11].

Highly energetic flow environments regularly contain non-homogeneous flow fields with spatial variation occurring at scales smaller than the resolution of traditional ADCPs. This poses challenges to flow characterisation, generating uncertainty in the assessment of forces and loads operating on submerged structures in energetic flow environments.

High resolution measurement is required, for example, in applications such as the generation of electricity from turbines driven by tidal currents. The siting, design and operation of a marine hydrokinetic (MHK) turbine is heavily dependent on the local flow characteristics proximal to the turbine's rotor plane [12, 13] requiring measurement resolution of spatial scales equivalent to blade chord lengths on the order of 1 m [6]. MHK turbines are typically situated at elevations that allow the submergence of the rotor even in the presence of surface waves and above the low flow velocities near the sea floor and therefore commonly require remote measurements to capture the flow characteristics. Measurement range of acoustic sensors is governed by the acoustic frequency, acoustic signal form and processing technique, and site conditions. Remote measurement is possible at considerable and useful distances from the sensor's location, with the range of a 1200 and 600 kHz unit being of the order of 20 and 40 m, respectively. Other scenarios of high spatial variability in a velocity flow field include the short convergent intake structure typical of most low-head Kaplan turbine hydropower plants. The non-homogeneous flows in both the forebay [14] and the intake structures [15] also represent flow environments which require greater measurement resolution than that offered by a conventional ADCP.

The acoustic Doppler velocimeter (ADV) is another flow measurement device based on the principle of the Doppler shift: a high frequency, high precision, point velocimeter which operates in a convergent beam configuration with a small sample volume ($\sim$1 cm^3) in close proximity to the instrument (between 50 and 100 mm). ADVs are extensively applied in the laboratory to obtain information on mean and turbulent flows upstream and downstream of model turbines (e.g. [16]) or to investigate the effect of wave-current interactions on a model MHK (e.g. [17, 18]). Recent advances in inertial measurement unit (IMU) integration has allowed the deployment of ADVs on compliant moorings to obtain high-precision measurements in the water column [19–21].

1.2. Convergent-beam acoustic Doppler velocimetry

The current research targets improved flow measurement resolution using remote measurement technology based on a
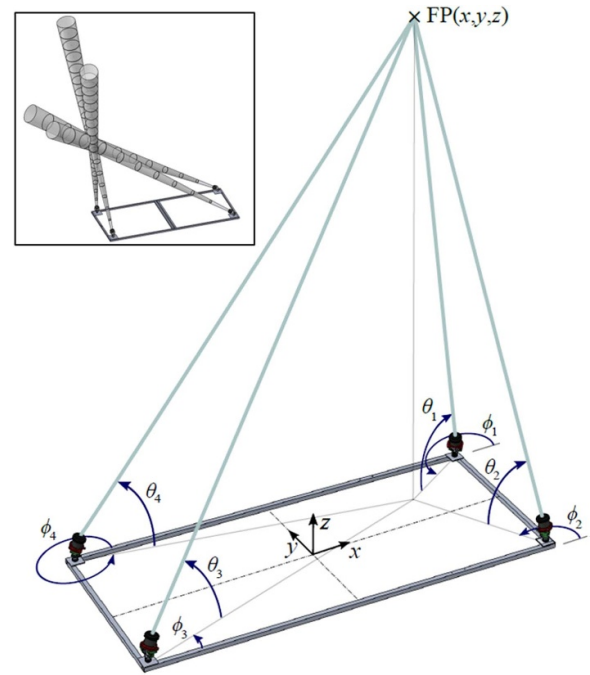
Figure 1. Definition of C-ADP coordinate system, and yaw and pitch angle directions used in the transform from beam to instrument coordinates. Inset of alternative beam orientation and focal point achieved using actuated control of the acoustic beam direction.

modified configuration of conventional ADCP technology. Unlike the standard configuration, in which multiple acoustic beams geometrically diverge from a single instrument, the new sensor comprises multiple spatially separate instruments. Each instrument features a single acoustic beam that is directed towards a remote focal point where the beams intersect. Each single beam has a beam spread angle from cone wall to beam axis of 1.45°. For the purposes of this paper, the beam intersection location is termed the focal point. By directing the acoustic beams in a converging arrangement, the sample volume where the three dimensional velocity estimate can be derived (at the focal point and remote region of interest) is significantly decreased, reducing reliance on the standard assumption of flow homogeneity and reducing uncertainty in instantaneous flow measurements. The new sensor realises a sample volume at the focal point of 0.03 m^3, compared to a standard divergent ADCP where the level of spatial averaging increases with distance from the transducer with a spatial resolution ranging from approximately 0.4 to 20 m^3. For comparison, an ADV sample volume is 2×10^{-6} m^3. The geometrically-converging sensor configuration is termed the converging acoustic Doppler profiler (C-ADP).

Earlier developments of the C-ADP concept have been presented by Sellar *et al* [22] and Hay *et al* [23]. Sellar *et al* [22] validated a C-ADP installed on the nacelle of an operational tidal turbine at the European Marine Energy Centre (EMEC), Orkney, UK by comparison to a proximal conventional ADCP and a vertical acoustic Doppler profiler. The converging profiler comprised a fixed, symmetrical beam geometry (with a sensor footprint of approximately 3.5×1.5 m)

that provided high resolution flow measurements at a focal point located 4 m above the sensor system. With a system deployed in the Bay of Fundy, Canada, [23] used a bistatic configuration to enable acquisition of pulse-to-pulse coherent velocity measurements and increase velocity precision. Validation utilised a co-located ADV on a fixed tripod mount.

1.3. Towards 3D flow-volume scanning

In this study, the C-ADP sensor system has been advanced by integrating and demonstrating the capability of 3D positional control of the focal point location. This is achieved by mounting each acoustic instrument on an electro-mechanical actuator with two degrees of freedom (yaw and pitch), as shown in figure 1. With this arrangement, velocity measurements can be achieved at multiple locations within and outside the frame's footprint. The current experiment explored the fluid volume of approximately $3 \times 3 \times 5$ m.

The 3D-volumetric scanning C-ADP concept was conceived during the ReDAPT project and the potential consequences of asymmetric beam geometry introduced in Harding *et al* [24]. The work discussed in this paper will inform the next iteration of the C-ADP; a large scale seabed sensor that is under-development within the European funded, Horizon 2020 *RealTide* project. The implementation presented herein, is to the authors' knowledge, the first publication of remotely measured flow velocity results from acoustic measurements at an off-axis remote focal point, the location of which can be programmatically adjusted through actuation.

1.4. Article layout

This paper begins with the derivation of the generalised coordinate transform to calculate a 3D velocity vector from the four converging acoustic beams of the C-ADP (section 2.2). Subsequently, the experimental configuration and associated prototype instrumentation are presented with an overview of the field test campaign conducted at the Pacific Northwest National Laboratory (PNNL) Marine Sciences Laboratory, Sequim, Washington State, USA. Initial sensor system validation is described via comparison of C-ADP velocity measurements to proximal, motion-corrected ADV velocity measurements at nine sensing locations.

2. Methodology

2.1. Co-ordinate system

The C-ADP comprises multiple single-beam acoustic Doppler profiler (s-ADP). Each s-ADP measures the component of velocity in the direction of the acoustic beam. The beam-wise velocity of the *i*th beam is denoted as b_i, with the positive flow direction being defined as away from the transducer.

The instrument co-ordinate system of the C-ADP is defined relative to the centre of the frame, as shown in the schematic of figure 1. Here the *x*-direction is aligned with the longitudinal axis of the frame, the *y*-direction as orthogonal to the *x*-axis

on the plane of the frame, and the *z*-direction orthogonal to the *x*–*y* plane according to the right hand coordinate convention. The instantaneous Cartesian velocity components are aligned with the frame co-ordinate system and are denoted $\vec{u} = (u,v,w)$.

An s-ADP is installed on each corner of the frame and labeled from 1 to 4 as shown in figure 1, in accordance with the quadrant in which it is mounted.

2.2. Co-ordinate transformation

The co-ordinate transform builds on that of Sellar *et al* [22] which describes the case of a converging beam configuration focusing on a fixed point where $x = y = 0$.

The positive angle of yaw (ϕ) is defined as counterclockwise from the *x*-axis and the positive angle of pitch (θ) is defined from the *x*–*y* plane, as shown in figure 1 for each s-ADP.

The components of the Cartesian velocities captured in each acoustic beam velocity component is presented in equation (1) where *i* represents the instrument number:

$$b_i = u\cos\phi_i\cos\theta_i + v\sin\phi_i\cos\theta_i + w\sin\theta_i. \tag{1}$$

For the 4-beam C-ADP, the resulting set of equations are presented in matrix form in equation (2):

$$\mathbf{b} = \mathbf{R} \cdot \vec{u},$$
$$\text{where } \mathbf{b} = \begin{bmatrix} b_1 & b_2 & b_3 & b_4 \end{bmatrix}^{\mathbf{T}},$$
$$\mathbf{R} = \begin{bmatrix} \cos\phi_1\cos\theta_1 & \sin\phi_1\cos\theta_1 & \sin\theta_1 \\ \cos\phi_2\cos\theta_2 & \sin\phi_2\cos\theta_2 & \sin\theta_2 \\ \cos\phi_3\cos\theta_3 & \sin\phi_3\cos\theta_3 & \sin\theta_3 \\ \cos\phi_4\cos\theta_4 & \sin\phi_4\cos\theta_4 & \sin\theta_4 \end{bmatrix}, \tag{2}$$
$$\text{and } \vec{u} = \begin{bmatrix} u & v & w \end{bmatrix}^{\mathbf{T}}.$$

The vector transformation matrix from beam to C-ADP instrument coordinates is therefore calculated as $\vec{u} = \mathbf{R}^{-1}\mathbf{b}$. Because the transformation matrix, $\mathbf{R}$, is not a square matrix, the inverse is calculated as the Moore–Penrose pseudoinverse to solve for this system of linear equations, equivalent to a least-squares solution.

The magnitude of the 3D velocity vector ($v = \|\vec{u}\|$) was used in the comparison of the C-ADP measurement with the ADV measurement in this paper.

2.3. Instrument assembly

The C-ADP was initially assembled at the PNNL Richland campus, Washington State, USA where the acoustic and actuation units were mounted on the frame (figure 2), described in the following sections.

2.3.1. Frame construction.
The C-ADP prototype frame was fabricated from 50 mm box section aluminium, measuring 4.9 m in length by 2.0 m in height, shown in figure 2(a). Square aluminium plates were added to each corner for the mounting of the actuation units. Additional stiffness was provided by bracing elements fabricated using additional aluminium box
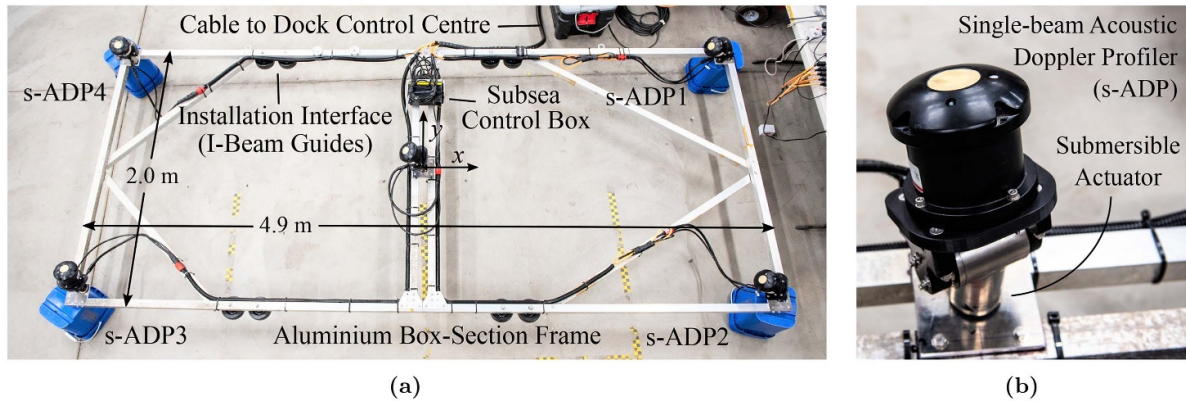
Figure 2. (a) Prototype C-ADP frame of length 4.9 m and width 2.0 m. (b) Close-up view of an s-ADP mounted on an actuator.

Figure 3. Attainment of two focal points at a solid boundary (target range = 8 m). Demonstrated via convergence of five spotlight beams, each with beam spread angle greater than that of s-ADP, mounted on the C-ADP's 5 actuation units. Image taken in two shots and overlaid, beam schematic superimposed. Conducted during laboratory commissioning and verification of control software.

section. Zinc anodes were fitted to provide anodic corrosion protection.

2.3.2. Actuation. Directional control of the acoustic instruments used Arctic Ray *Hammerhead* 'pan and tilt' units. These rotational actuators are compact, subsea, air-filled positioners, rated for 1000 m depth with 6.8 N-m of torque. The actuators were mounted on the C-ADP frame such that the yaw (pan) axis was aligned with the z-axis. Each actuator unit contained an absolute encoder which measured the rotational position of each axis to $0.2°$ accuracy, used in the proportional position controller. Each actuator was connected via an individual cable to a dry box which converted

RS-485 serial communications to Ethernet and provided 28 V DC power.

2.3.3. Acoustic sensors. The s-ADP used on the prototype were 1 MHz Nortek AD2CP units previously used in the field trials described by Sellar *et al* [22]. These transducers were mounted to the actuators using ABS brackets as shown in figure 2(b). Five s-ADP units were installed on the frame, with the results of the four corner units reported in this paper. Each s-ADP was cabled into a subsea control box that was fixed onto the frame. A single 24 V DC power and Ethernet cable ran from the control box to the control computer.

Each transducer had independently controllable time offset referenced to a timing signal supplied by a GPS Grandmaster clock (providing IEEE 1588 PTP timing). This enabled offsetting of the transmission of each acoustic signal to within microsecond accuracy, allowing asynchronous transmission of acoustic signals [22]. The instruments were operated in mono-static mode with each instrument transmitting and receiving its own signal. This mode of operation requires asynchronous signal transmission sequencing to reduce instrument-to-instrument interference [22]. The data record is integrated with the time stamp, permitting collation and analysis in post-processing of the data from each s-ADP.

2.3.4. System functionality verification. The frame, s-ADP instruments and actuator units were assembled and calibrated, and the actuation proportional control software tested in the laboratory. For each user selected focal point, a MATLAB-based simulation of the C-ADP was used to calculate the required direction of each beam and the blanking distance and cell size of the s-ADP. A digital inclinometer was used to validate the control and alignment of the actuator units. The functionality of the directional calculation and control system was verified via the installation of narrow-beam spotlights onto the units using removable brackets (figure 3). By visually inspecting the motion, position and degree of overlap of the light-pattern it was confirmed that the measured installation positions and angles of all of the individual s-ADP and actuator platforms were correct.
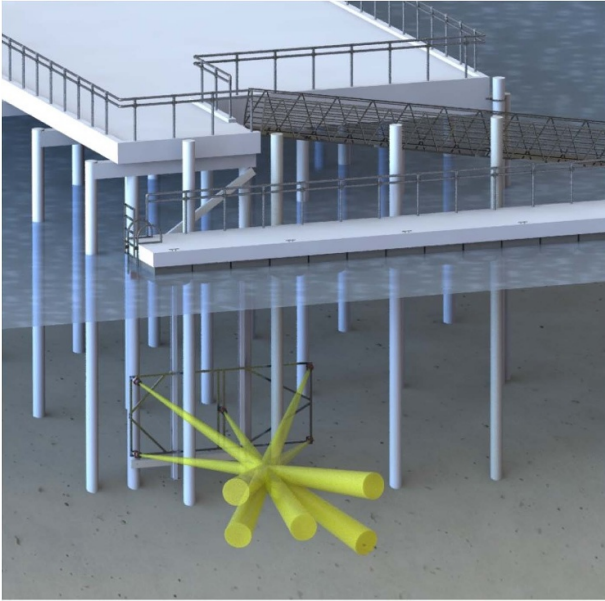
Figure 4. Schematic view of the C-ADP mounted on the end of the MSL Dock, Sequim, WA. The acoustic beams are highlighted in yellow. The floating dock, at the end of the ramp, was accessible during field testing to facilitate maintenance and ADV measurements.

2.4. Field deployment

The actuators and acoustic instruments were removed for transport and re-assembled on the frame at the Marine Sciences Laboratory dock of PNNL, Sequim, Washington State (48° 4′44′′N 123° 2′42′′W). The complex flow environment proximal to the dock is described in [25]. A schematic of the deployed C-ADP frame on the end of the dock is shown in figure 4. Power and communications for the C-ADP were cabled from a mobile office on the dock.

The frame was deployed down two parallel 5.5 m I-beams attached vertically to the fixed section of the dock. An electric winch deployed the frame to its operational depth and retrieved it periodically during the test period. Four pairs of plastic wheels (figure 2(a)) guided the frame down the I-beam rails, with adjustable spacing to avoid frame motion under high flow conditions. The frame was deployed to end stop on the I-beam with return to this position verified after each retrieval. Measurements were carried out from 23rd July to 7th August 2019. This test schedule targeted focal points across the ranges of -1.5 m $\leqslant x \leqslant$ 1.5 m, -0.75 m $\leqslant y \leqslant$ 1.5 m and 3.21 m $\leqslant z \leqslant$ 8.0 m. As shown by [22], velocity above and below the focal point can be calculated using the same coordinate transform as used at the focal point where the system operates as per a standard ADCP. This paper focuses on the results measured at the focal point as the location of maximum spatial resolution. This paper reports on a representative data set from the test schedule, collected on the 04 August 2019, from locations in the x–y plane at $z = 3.21$ m, within the ranges of -1.5 m $\leqslant x \leqslant$ 1.5 m and -0.75 m $\leqslant y \leqslant$ 1.5 m. Over the measurement period, tidal velocities were recorded of between 0.4 and 0.7 m s^{-1}.
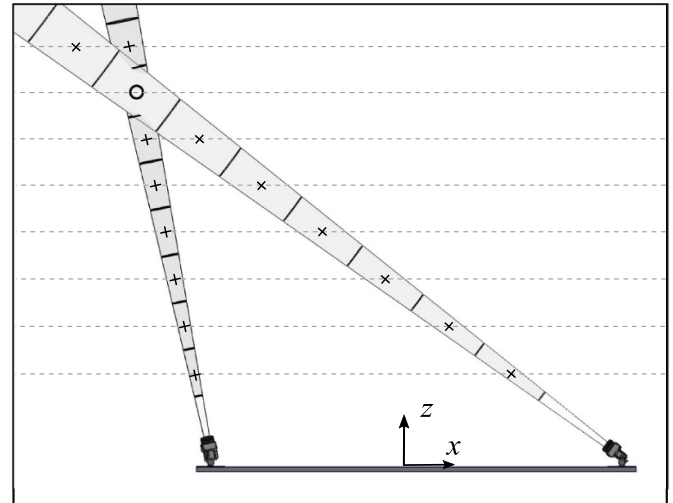
Figure 5. Schematic view of the acoustic beams and cell centres (marked with $+$ symbol) in the x–z plane, demonstrating that each beam requires distinct blanking distance and cell size to achieve regular profile measurement spacing in the z-direction. The focal point is indicated with a black circle.

2.4.1. Deployment configuration. To control the direction of each acoustic beam to intersect the focal point, the yaw (ϕ) and pitch angles (θ) are calculated for each beam. Unlike conventional ADCPs where each beam has the same blanking distance (BD) and cell size (CS), BD and CS are calculated for each beam to achieve regular bin spacing in the z-direction (figure 5). The minimum BD and CS were constrained to always exceed a value of 0.4 m, the minimum to which the instrument could be set.

A summary of the key deployment configuration variables used in this study are presented in table 1. Additionally, all s-ADPs sampled at a frequency of 2 Hz and were configured with an ambiguity velocity of 2 m s^{-1}. Settings were informed by previous field deployments of the s-ADP in a convergent configuration [22].

2.5. Preliminary validation measurements

To obtain preliminary validation of the flow velocity measurements acquired by the 4-beam C-ADP, an ADV was co-deployed on a 27 kg, streamlined sounding weight platform. The ADV was a 6 MHz Nortek Vector with IMU motion correction. The ADV was deployed in self-contained mode with the cabled ADV head being installed in an upward looking orientation at the nose of the sounding weight. The deployment guidelines provided by Kilcher *et al* [26] were followed and integration of an inertial measurement unit enabled the motion of the tethered ADV to be removed in Python using the *dolfyn* library [20]. The RMS velocity of the removed ADV motion was less than 0.1 m s^{-1} in all data reported.

Co-location of the ADV sample volume and the C-ADP focal point led to interference with the velocity measurement of the C-ADP as the ADV and the sounding weight assembly caused high signal amplitude return. Preliminary tests showed

Table 1. Deployment configuration used in field validation experiments of the C-ADP prototype.

	Beam 1	Beam 2	Beam 3	Beam 4
Actuator mounting points (x,y) (m)	(2.24, 0.89)	(2.24, −0.89)	(−2.24, −0.89)	(−2.24, 0.89)
Focal point locations (m)		$-1.5 \leqslant x \leqslant 1.5$; $-0.75 \leqslant y \leqslant 1.5$; $z = 3.21$		
Yaw angle (°)	$90 \leqslant \phi_1 \leqslant 270$	$90 \leqslant \phi_2 \leqslant 180$	$0 \leqslant \phi_3 \leqslant 90$	$-90 \leqslant \phi_4 \leqslant 90$
Pitch angle (°)		$30 \leqslant \theta \leqslant 90$		
Transmit offset (Δt) (ms)	0	24	48	72

Table 2. Calculation of ADV location in *y*-direction for field validation experiments of the C-ADP prototype. References illustrated schematically in figure 6.

	Reference	Descriptor
Constant inputs	A	Top of I-Beam to top of C-ADP frame
	B	Top of C-ADP frame to $y = 0$
	D	Focal point to ADV sample volume (1.0 m)
	E	ADV sample volume to coupling shackle
Variable inputs	C	$y = 0$ to focal point
	F	Top of I-Beam to water level
Calculated output	G	Water level to coupling shackle ($G = A + B + C - D - E - F$)

Figure 6. Schematic of ADV sample volume location in *y*-direction relative to C-ADP focal point, not to scale (references contained within table 2).
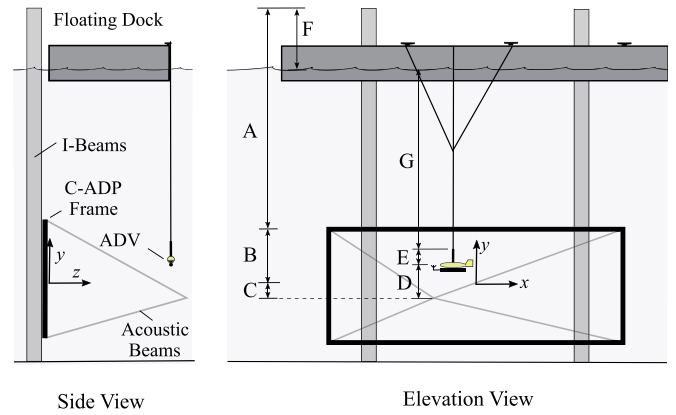
that locating the ADV sample volume to within approximately 1.0 m radius in the above and downstream direction of the C-ADP focal point captured similar flow behaviour while minimising interference of the ADV sounding weight both with the measured flow and with the acoustic beams at the C-ADP focal point. ADV sample volume positioning in the *x*-direction was achieved by adjusting the deployment location of the ADV along the floating dock. Inputs utilised to achieve positioning in the *y*-direction are presented in table 2 and figure 6. A sounding weight configuration was used to point the ADV head into the flow and to orient the head upstream of the sounding weight. ADV location was adjusted between measurement periods to accommodate changes in the relative locations of the ADV and C-ADP sample volumes given changes in C-ADP focal point location (dimension C in figure 6) and in tidal elevation (dimension F in figure 6).

The error between a metric calculated by the C-ADP and a reference instrument is defined by equation (3) where *R* denotes the reference measurement of the ADV and *υ* denotes velocity magnitude:

$$e_\upsilon = \upsilon_{\text{CADP}} - \upsilon_R. \qquad (3)$$

2.6. Data processing

Prior to analysis, a quality assurance process was conducted on a beam by beam basis for the C-ADP data. The following sequence of methods was applied to identify and remove spurious data:

Correlation threshold: Data points with correlation values less than 50%. This typically flagged less than 1% of the data.

Amplitude threshold: Data points with amplitude returns greater than 70 dB. This typically flagged less than 1% of the data.

Phase-space method: Velocity measurements as identified by application of the phase-space method based on [27]. This typically flagged less than 2% of the data.

This process was applied to data from the focal point measurement cell of each of the 4 acoustic beams of the C-ADP prior to the coordinate transform to calculate Cartesian velocity components described in section 2.2. Representative effects of filtering are illustrated in figure 7.

The phase space method was applied to measurements of each velocity component of the ADV data. This typically flagged less than 1% of the data.

3. Results

This paper focuses on a representative data set, collected on the afternoon of 4 August 2019. A number of locations were sampled in the *x*–*y* plane at $z = 3.21$ m, within the ranges of -1.5 m $\leqslant x \leqslant 1.5$ m and -0.75 m $\leqslant y \leqslant 1.5$ m. Measurements were made for a period of 10 minutes at each focal point location.

The time series of the velocity magnitude measured by both instruments is shown in figure 8. These plots are arranged according to their measurement location in the *x*–*y* plane. The
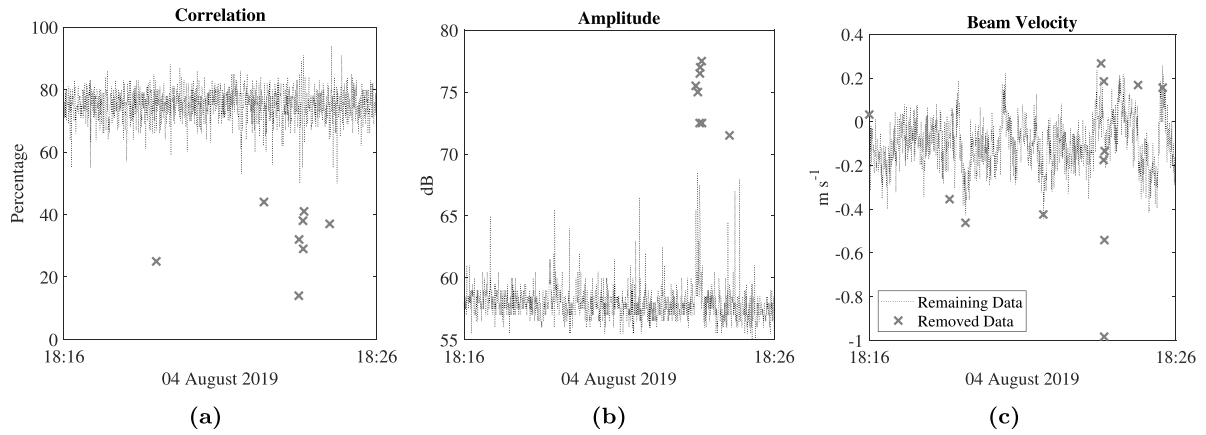
Figure 7. Example filtering of s-ADP instrument data: (a) correlation, (b) amplitude, and (c) beam velocity, with the × showing data removed by the respective filters.

ADV measurement is down-sampled to be synchronised to the C-ADP time stamp at a frequency of 2 Hz through ensemble averaging with an ensemble period of $t_e = 0.5$ s. A portion (4 min) of the full 10 min test duration is presented to aid visualisation of the measurements obtained by the C-ADP and the ADV.

A summary of the mean difference obtained between the ADV and C-ADP using $t_e = 0.5$ s is shown in table 3 for focal point measurements made at $z = 3.21$ m, within the ranges of -1.5 m $\leqslant x \leqslant 1.5$ m and -0.75 m $\leqslant y \leqslant 1.5$ m. These metrics show that mean velocity error varied within the range of $-0.083 \leqslant \overline{e_v} \leqslant -0.003$ m s^{-1}. The standard deviation of the velocity error exhibited a small range of $0.09 \leqslant \sigma_{e_v} \leqslant 0.12$ m s^{-1}.

Figure 9 shows the time series of the ADV and C-ADP in box-plot format and arranged in pairs by co-located test run. Tests are identified via the inset graph showing varied focal point (measurement) location. The velocity magnitudes from the separate instruments are in good agreement showing similar medians, means and standard deviations. The level of agreement is further quantified in figures 10 and 11. It is apparent in figure 9 that tests corresponding to focal points at $x = 1.5$ m are in poorer agreement compared to the others, which is also clearly evident in subsequent plots.

Figure 10 presents a comparison of the mean of the ADV and C-ADP velocity magnitudes for each of the nine measurement locations. A line of equality is also shown. Figure 11 presents the comparison of the two instruments (implemented and formatted as per Bland and Altman [28]), showing absolute error in velocity magnitude versus the aggregate mean of the velocity magnitude measured by the two sensors. It is shown that during these tests mean velocity magnitude ranged from 0.4 to 0.7 m s^{-1} across an x–y plane at a remote distance of 3.21 m from the sensor system. Average variation in v, across the nine tests, is shown to be approximately 6 cm s^{-1}. Two tests appear to have higher levels of disagreement (apparent in both figures 10 and 11). These correspond to focal-points at $x = 1.5$ m and increase overall variation levels, resulting in a group bias of approximately 3 cm s^{-1}. Velocity

measurements of the ADV consistently exceed that of the C-ADP.

A comparison between the velocity magnitude measured using the C-ADP and the ADV for a selected off-central-axis measurement location is presented in figure 12. These plots show a representative 10 min of flow data, measured at the focal point of $(0, 1.5, 3.21)$ m. The data was selected from the set of focal point locations as an indicative case study with representative mean velocity error and cross correlation (section 3.1). The left hand column of plots contains a comparison of raw C-ADP data which was collected at a frequency of 2 Hz and ADV data ensemble averaged with an ensemble duration, $t_e = 0.5$ s, such that the time stamp is synchronised. The right hand column of data shows the same comparisons with ensemble averaged data, $t_e = 10$ s.

Figures 12(a) and (b) show the C-ADP measurements tracking the ADV measurements in the time series, a trend that is confirmed by the direct comparison (1:1) plots of figures 12(c) and (d). Figures 12(e) and (f) show the normal distribution of the error velocity, with the mean indicating C-ADP underestimation of flow velocity relative to the reference ADV, in this example by 0.023 m s^{-1} when $t_e = 0.5$ s. Figure 12(e) is illustrative of the data summarised in table 3 for the case of FP $= (0, 1.5, 3.21)$ m.

3.1. Normalised cross-correlation

Cross-correlation provides a measure of similarity between two signals. In this analysis, the normalised cross-correlation coefficient of the velocity magnitude measured by the C-ADP and ADV time series, $\hat{R}_{v_1 v_2, \text{coeff}}$, was calculated at each focal point on data from which the mean had been removed (table 4). The normalising process allows the temporal similarity of the two time series to be described with a coefficient whereby identical signals return a value of 1. Over the range of focal point locations measured in this study, the cross correlation coefficient varies within the range of $0.51 \leqslant \hat{R}_{v_1 v_2, \text{coeff}} \leqslant 0.77$, ensemble period $t_e = 0.5$ s.

Table 3. Mean velocity error, $\overline{e_v}$, and standard deviation of the velocity error, σ_{e_v}, at multiple focal point locations ($z = 3.21$ m) with an ensemble period of $t_e = 0.5$ s. All error values are presented in units of m s^{-1}.

$\overline{e_v}\ (\sigma_{e_v})$		x (m)				
		−1.5	−0.75	0	0.75	1.5
y (m)	1.5			−0.023 (*0.092*)		−0.083 (*0.099*)
	0.75			−0.011 (*0.096*)		
	0	−0.023 (*0.123*)	−0.003 (*0.113*)	−0.011 (*0.101*)	−0.038 (*0.116*)	−0.075 (*0.088*)
	−0.75			−0.007 (*0.109*)		
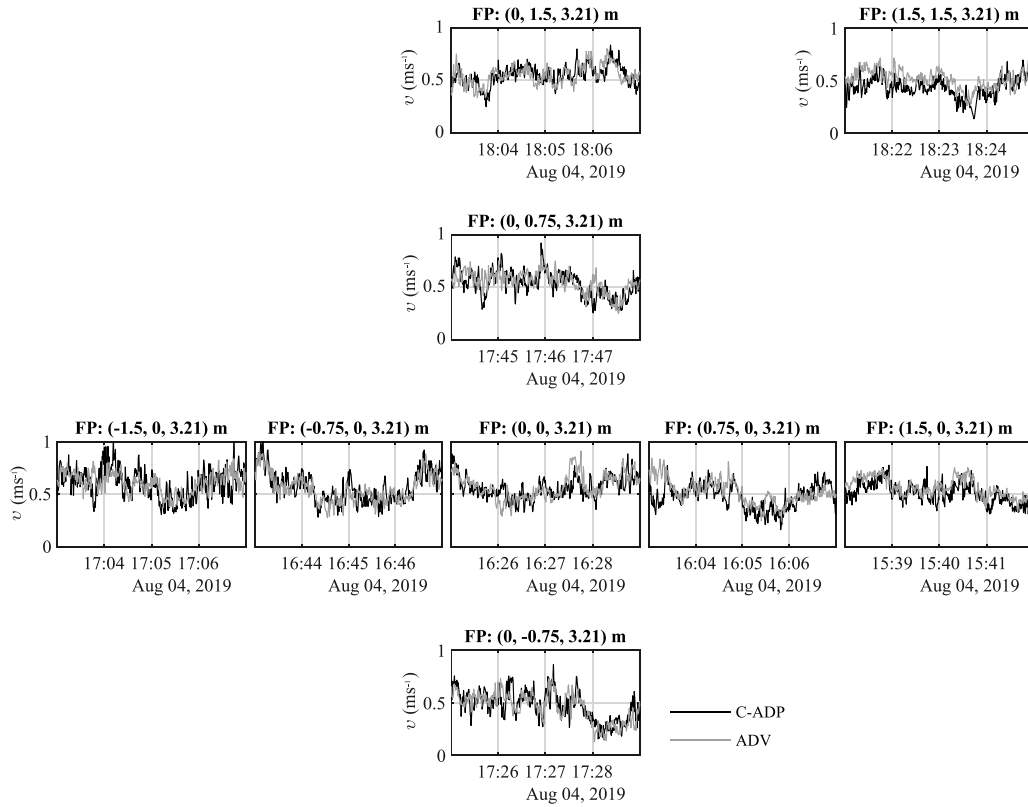
Figure 8. Time series of C-ADP and ADV for each location, measured during flood tide on 4 August 2019. The raw C-ADP results are shown and the ADV time series is ensemble averaged such that both time series are at a frequency of 2 Hz with a synchronised time stamp. For clarity, 4 min of the available 10 min data set is shown in each case.

Table 4. Normalised cross correlation between C-ADP and ADV velocity measurements at multiple focal point locations ($z = 3.21$ m) with an ensemble period of $t_e = 0.5$ s (left) and $t_e = 10$ s (right).

$\hat{R}_{v_1 v_2,\mathrm{coeff}}$		x (m)				
		−1.5	−0.75	0	0.75	1.5
y (m)	1.5			0.658–0.845		0.483–0.643
	0.75			0.616–0.821		
	0	0.542–0.779	0.638–0.854	0.634–0.845	0.520–0.720	0.576–0.830
	−0.75			0.749–0.927		

The increase in cross-correlation as a function of ensemble period is shown in figure 13, which demonstrates a representative relationship that applies to all other measurement locations (table 4). An ensemble period of $t_e = 0.5$ s, corresponding to the raw C-ADP data frequency, results in a cross-correlation coefficient of $\hat{R}_{v_1 v_2,\mathrm{coeff}} = 0.66$ for the representative focal point location of (0, 1.5, 3.21) m. This is seen to increase to

value of $\hat{R}_{v_1 v_2,\mathrm{coeff}} = 0.83$ with an ensemble period of $t_e = 10$ s and to $\hat{R}_{v_1 v_2,\mathrm{coeff}} = 0.95$ at an ensemble period of $t_e = 60$ s.
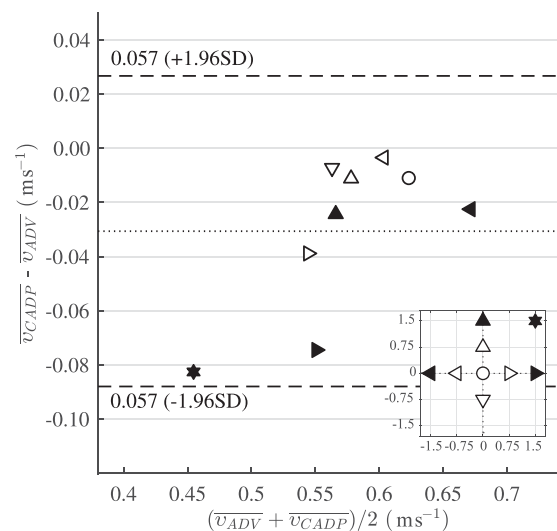
3.2. Root mean squared error

The increase in the level of agreement with increasing ensemble averaging time period is also apparent from the
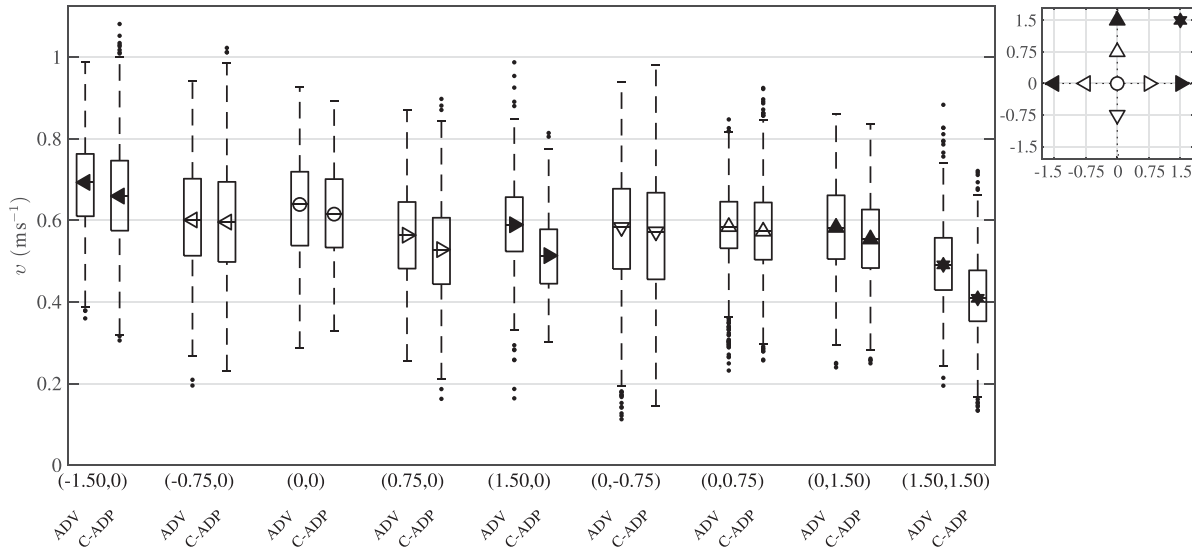
Figure 9. Box-plots of ADV and C-ADP velocities (magnitude) for nine focal-points. Markers within boxes show sample median values, box-edges are the 25th and 75th percentiles, the whiskers extend to the most extreme data points, and outliers are plotted individually. Inset: Location of focal point per test in frame coordinates (m).
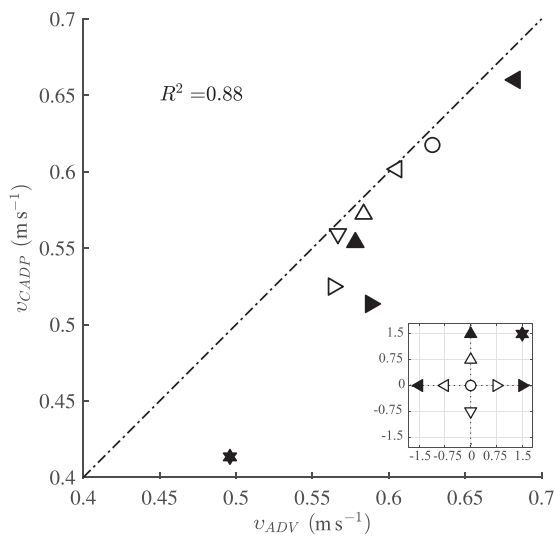
Figure 10. Comparison of ADV and C-ADP mean velocity magnitudes. Inset: Location of each of the nine focal points.

Figure 11. Comparison of absolute error vs mean of ADV and C-ADP measurements. Inset: Location of each of the nine focal points.

decreasing root-mean-squared error (RMSE) when comparing υ between the C-ADP and ADV values, as shown in figure 13. A power-law fit has been included to aid visualisation of the trend. RMSE decreases rapidly up to $t_e = 20$ s before falling at a reduced rate to approximately 0.025 m s^{-1} at ensemble periods above $t_e = 60$ s.

4. Discussion

The novel flow measurement instrument presented in this paper expands research that validated the C-ADP concept for a fixed beam geometry [22]. The relatively small sample volume at the focal point reduces uncertainty in flow measurements

caused by the assumption of homogeneity between beams in a diverging beam configuration.

Initial results demonstrate that the calculation of beam directions to achieve a specified focal point location has been executed successfully. Control of the actuated units in two rotational degrees of freedom (yaw and pitch) enabled the focal point to be adjusted to a range of target locations. Preliminary analysis of the current measurements obtained by the C-ADP were validated against synchronous ADV measurements. The results presented show the agreement obtained between the time series C-ADP and ADV measurements at each of nine focal points in the *x–y* plane at $z = 3.21$ m, within the ranges of -1.5 m $\leqslant x \leqslant 1.5$ m and -0.75 m $\leqslant y \leqslant 1.5$ m.
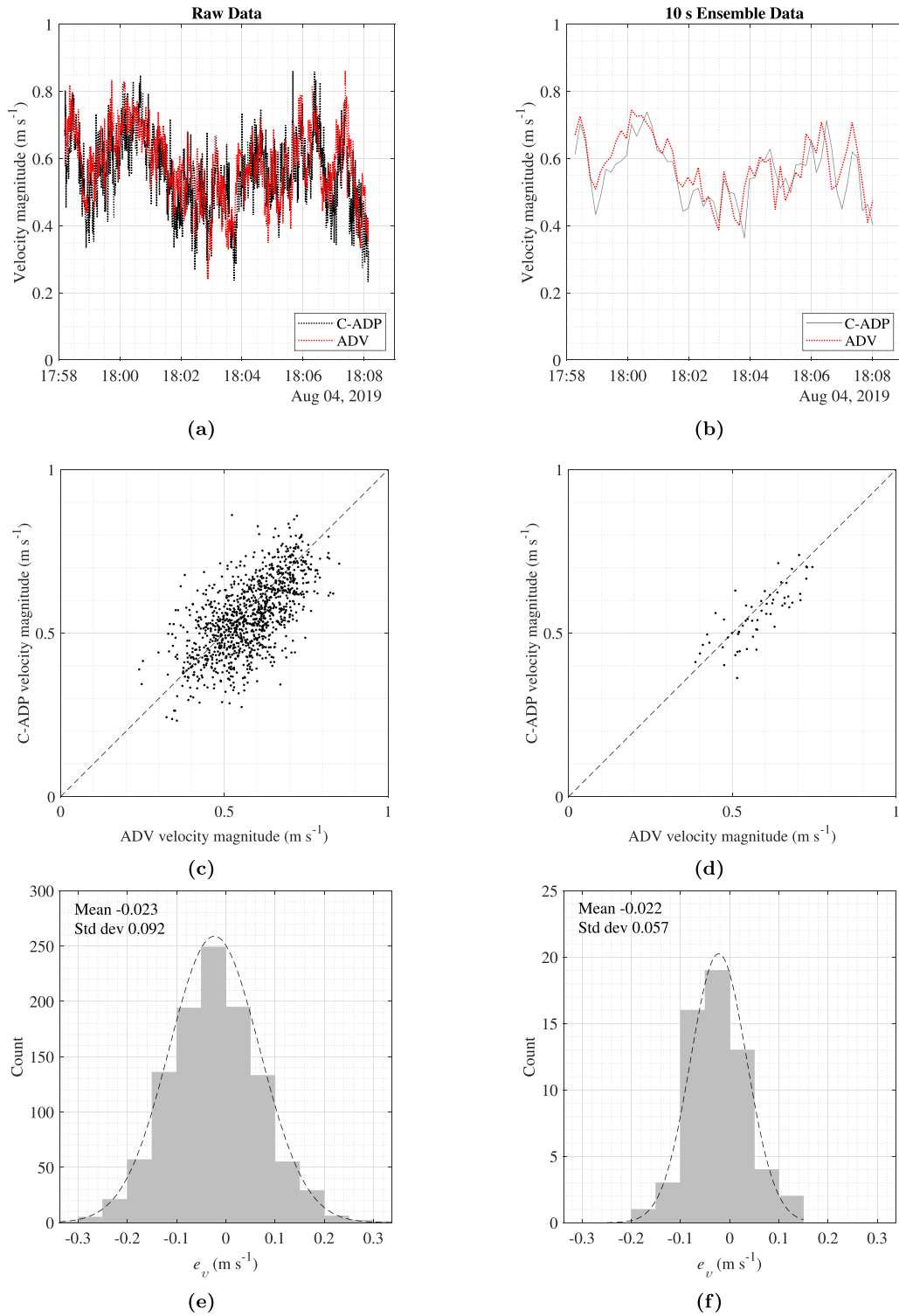
Figure 12. Comparison between C-ADP and ADV data for a 10 min time period at off-axis focal point of FP = (0, 1.5, 3.21) m. Time series of ADV and C-ADP data (a), (b); direct comparative plot of velocity magnitude (c), (d); histogram of error distribution with bin width of 0.05 m s^{-1} and a normally fitted distribution indicated by the dashed black line. Text indicates mean velocity error, $\overline{e_v}$, and standard deviation of the velocity error, σ_{e_v} (e), (f). Data shown at a frequency of 2 Hz in the left hand column and at 0.1 Hz in the right hand column by applying ensemble averaging at $t_e = 0.5$ s and $t_e = 10$ s, respectively.

This comparison, across a range of experienced tidal velocities of 0.4–0.7 m s^{-1}, showed a mean velocity error, across all sampled locations, of $-0.080 \leqslant \overline{e_v} \leqslant -0.001$ m s^{-1}. This indicates that on average the ADV measured higher values than the C-ADP (equation (3)).

Cross-correlation of the velocity signals from the ADV and the C-ADP is seen to increase with longer averaging periods.
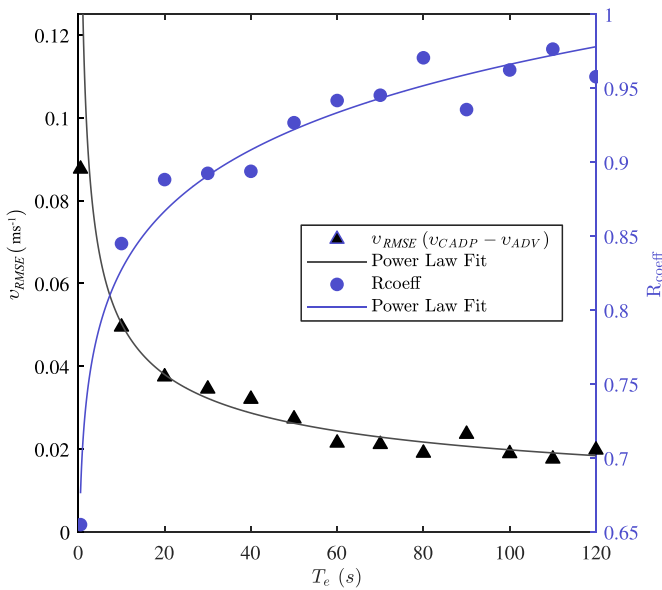
Figure 13. Cross-correlation coefficient, $\hat{R}_{v_1 v_2,\text{coeff}}$ (blue circles) and RMSE of v (black triangles) as a function of temporal ensemble averaging period, t_e. Power law fits highlight the trend of increasing agreement between sensors with increasing ensemble period.

This is both a result of temporal averaging which removes the standard error from the signal, as well as spatial averaging effects which result from temporal averaging in moving flow. Though a value of unity indicates identical, this was not expected for these comparisons as the two measurement locations were required to be spatially separated to avoid sensor-to-sensor interference. This separation precludes a conclusion being reached on an acceptable threshold for agreement between the sensors.

Despite this, obtaining velocities and correlations with equivalent trends across measurements from all nine focal points suggests the ability of the sensor to measure flow velocities at multiple points within the C-ADP scanned volume of $3 \times 3 \times 5$ m.

It is notable that two of the nine sampled locations return data with significantly larger differences in the mean between instruments (figures 10 and 11), which strongly affects the overall group bias and variation. A relative error of less than 5% was returned for measurements where $x \leqslant 0$ whereas relative error of 13.2% and 11.2% occurred at FP $=$ (1.5, 1.5, 3.21) m and FP $=$ (1.5, 0, 3.21) m respectively. The cause of these larger discrepancies remains under investigation. The differences are potentially attributable to the experimental set-up, with interference between Beam 3 and a proximal jetty pile distorting C-ADP velocity measurement at locations where $x > 0$. This is illustrated schematically in figure 14(a) for FP $=$ (0, 0, 3.21) m relative to FP $=$ (1.5, 0, 3.21) m and supported by figure 14(b) which presents the mean amplitude return over the measurement period for Beams 2 and 3 at these two focal point configurations. Across the measurement range, Beam 3, FP $=$ (1.5, 0, 3.21) m is associated with a lower amplitude return compared to Beam 3, FP $=$ (0, 0, 3.21) m. It is suggested that the high amplitude spike typically observed from

hard scatterer interference occurred in the blanking distance of Beam 3, FP $=$ (1.5, 0, 3.21) m, however the 'deficit' following the interference is evident (figure 14(b)) when compared to FP $=$ (0, 0, 3.21) m.

5. Conclusions

This paper has presented the development and testing of a C-ADP with a remote focal point, the location of which can be programmatically adjusted through actuation. This novel flow measurement instrument, based on standard acoustic velocimetry, samples a remote measurement location using multiple acoustic beams with independent directional control. The successful calculation and control of beam directions to achieve a specified focal point location was demonstrated in the laboratory. Sensor deployment from the Marine Sciences Laboratory dock of PNNL, Sequim, Washington State enabled the measurement of tidal flows and comparison between C-ADP and synchronous ADV measurements.

Preliminary validation, whilst limited by the requirement for spatial separation between the focal points of the two sensors, demonstrated C-ADP performance at the flow speeds under test. Inter-sensor agreement improved with increasing ensemble averaging time period, as expected given the extent of spatial variation and turbulence in the flow field.

6. Future work

The next iteration of the C-ADP improves the spatio-temporal resolution of measurements via the integration of the new generation of s-ADP units, based on the Nortek Signature 1000 platform. This iteration decreases the minimum measurement cell size, allows sample rates of up to 16 Hz and provides streamlined hardware control. These units are undergoing laboratory commissioning and are being integrated into a large scale seabed C-ADP as part of the *RealTide* project.

The configuration of the C-ADP discussed in this paper provides more than the minimum required three acoustic beams to resolve 3D velocity at the focal point. This redundancy provides the opportunity to derive quality control metrics via consideration of multiple 3 beam solutions and of instantaneous flow measurements in specific directions using independent combinations of acoustic beams. Calculation of quality control metrics allows the flagging of poor data and selection of the highest quality combination of beams. This information can then be used to select only the beams contributing towards optimal levels of sensor performance, increasing the performance of the sensor across the range of focal points sampled throughout the scanned volume.

Acknowledgments
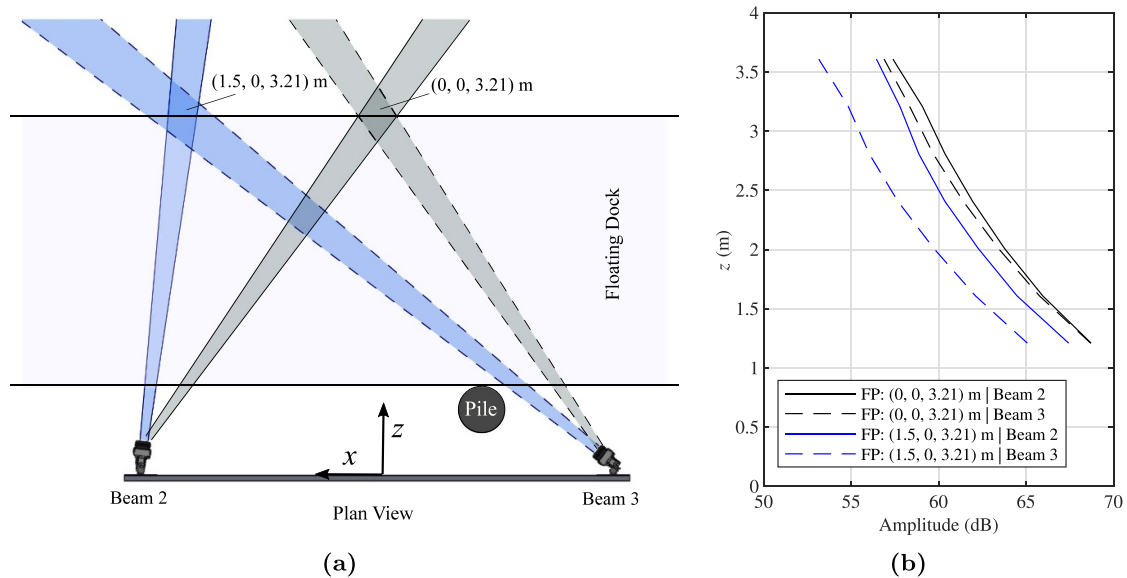
Figure 14. (a) Schematic of acoustic beams relative to interfering pile, shown in plan view with *x* positive left and (b) resulting signal amplitude effects.

ORCID iDs

Mairi Dorward ⬤ https://orcid.org/0000-0001-7010-4022
Brian Sellar ⬤ https://orcid.org/0000-0003-1683-0730

References

[1] Muste M, Yu K and Spasojevic M 2004 Practical aspects of ADCP data use for quantification of mean river flow characteristics. Part I: moving-vessel measurements *Flow Meas. Instrum.* **15** 1–16

[2] Szupiany R N, Amsler M L, Best J L and Parsons D R 2007 Comparison of fixed- and moving-vessel flow measurements with an ADP in a large river *J. Hydraul. Eng.* **133** 1299–309

[3] Youyu L and Lueck R G 1999a Using a broadband ADCP in a tidal channel. Part I: mean flow and shear *J. Atmos. Ocean. Technol.* **16** 1556–67

[4] Goddijn-Murphy L, Woolf D and Easton M 2013 Current patterns in the inner sound (Pentland Firth) from underway ADCP data *J. Atmos. Ocean. Technol.* **30** 96–111

[5] Youyu L and Lueck R G 1999b Using a broadband ADCP in a tidal channel. Part II: turbulence *J. Atmos. Ocean. Technol.* **16** 1568–79

[6] Thomson J, Polagye B, Durgesh V and Richmond M C 2012 Measurements of turbulence at two tidal energy sites in Puget sound, WA *IEEE J. Ocean. Eng.* **37** 363–74

[7] Togneri M, Lewis M, Neill S and Masters I 2017 Comparison of ADCP observations and 3D model simulations of turbulence at a tidal energy site *Renew. Energy* **114** 273–82

[8] Thiébaut M, Sentchev A and Bailly du Bois P 2019 Merging velocity measurements and modeling to improve understanding of tidal stream resource in Alderney Race *Energy* **178** 460–70

[9] Jeffcoate P, Starzmann R, Elsaesser B, Scholl S and Bischoff S 2015 Field measurements of a full scale tidal turbine *Int. J. Mar. Energy* (Special Issue on Marine Renewables Infrastructure Network) **12** 3–20

[10] Sentchev A, Thiébaut M and Schmitt Fçois G 2020 Impact of turbulence on power production by a free-stream tidal turbine in real sea conditions *Renew. Energy* **147** 1932–40

[11] Milne I A, Day A H, Sharma R N and Flay R G J 2016 The characterisation of the hydrodynamic loads on tidal turbines due to turbulence *Renew. Sustain. Energy Rev.* **56** 851–64

[12] Lewis M, Neill S P, Robins P, Hashemi M R and Ward S 12 2017 Characteristics of the velocity profile at tidal-stream energy sites *Renew. Energy* **114** 258–72

[13] Sellar B, Wakelam G, Sutherland D, Ingram D and Venugopal V 2018 Characterisation of tidal flows at the European marine energy centre in the absence of ocean waves *Energies* **11** 176

[14] Harding S, Richmond M, Romero-Gomez P and Serkowski J 2016a Effects of non-homogeneous flow on ADCP data processing in a hydroturbine forebay *Flow Meas. Instrum.* **52** 1–9

[15] Romero-Gomez P, Harding S and Richmond M 2017 The effects of sampling location and turbulence on discharge estimates in short converging turbine intakes *Eng. Appl. Comput. Fluid Mech.* **11** 513–25

[16] Tedds S C, Owen I and Poole R J 2014 Near wake characterisation of a model horizontal axis tidal stream turbine *Renew. Energy* **63** 222–35

[17] De Jesus Henriques T A, Tedds S C, Botsari A, Najafian G, Hedges T S, Sutcliffe C J, Owen I and Poole R J 2014 The effects of wave–current interaction on the performance of a

model horizontal axis tidal turbine *Int. J. Mar. Energy* **8** 17–35

[18] Draycott S, Payne G, Steynor J, Nambiar A, Sellar B and Venugopal V 2019 An experimental investigation into non-linear wave loading on horizontal axis tidal turbines *J. Fluids Struct.* **84** 199–217

[19] Harding S, Kilcher L and Thomson J 2017 Turbulence measurements from compliant moorings. Part I: motion characterization *J. Atmos. Ocean. Technol.* **34** 1235–47

[20] Kilcher L, Thomson J, Harding S and Nylund S 2017 Turbulence measurements from compliant moorings. Part II: motion correction *J. Atmos. Ocean. Technol.* **34** 1249–66

[21] McMillan J M and Hay A E 2017 Spectral and structure function estimates of turbulence dissipation rates in a high-flow tidal channel using broadband ADCPs *J. Atmos. Ocean. Technol.* **34** 5–20

[22] Sellar B, Harding S and Richmond M 2015 High-resolution velocimetry in energetic tidal currents using a convergent-beam acoustic Doppler profiler *Meas. Sci. Technol.* **26** 085801

[23] Hay A E, Zedel L, Nylund S, Craig R and Culina J 2015 The Vectron *2015 IEEE/OES 11th Current, Waves and Turbulence Measurement, CWTM 2015*

[24] Harding S, Sellar B and Dorward M 2019 Implications of asymmetric beam geometry for convergent acoustic Doppler profilers *2019 IEEE/OES 12th Current, Waves and Turbulence Measurement, CWTM 2019*

[25] Harding S F, Hall K D, Vavrinec J, Harker-Klimeš G E L, and Richmond M C 2016 Field characterization of triton tidal site: vessel-mounted ADCP survey of Sequim Bay Inlet *Technical Report* November

[26] Kilcher L, Thomson J, Talbert J, and Deklerk A 2016 Measuring turbulence from moored acoustic Doppler velocimeters: a manual to quantifying inflow at tidal energy sites *Technical Report* National Renewable Energy Laboratory NREL/TP-5000-62979

[27] Goring D and Nikora V 2002 Despiking acoustic Doppler velocimeter data *J. Hydraul. Eng.* **128** 117–26

[28] Bland J M and Altman D G 1986 Statistical methods for assessing agreement between two methods of clinical measurement *Lancet* **327** 307–10